Cell Reports
Physical Science

Article

2D photonic crystal emitter at 1,400°C for thermophotovoltaic energy harvesting

Graphical abstract

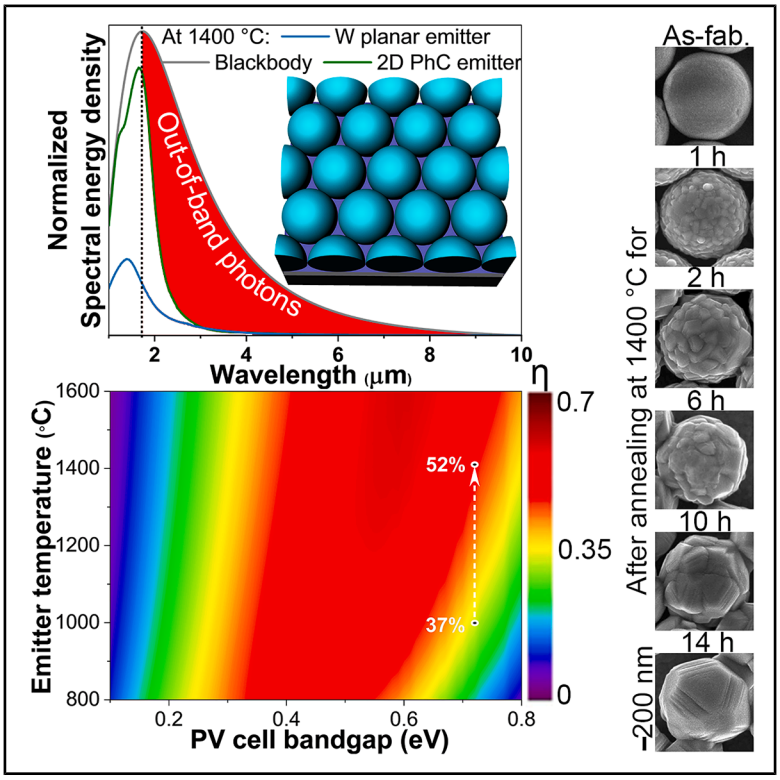

Highlights

- 2D photonic crystal emitters exhibit structural stability up to 1,400°C
- Long-term durability exceeds 6 months and 200 thermal cycles at 1,050°C
- Spectral efficiency reaches 52% at a 0.72 eV photovoltaic cell band gap
- Cost-effective, scalable fabrication enables robust TPV energy harvesting

Authors

Manohar Chirumamilla, Gnanavel V. Krishnamurthy, Yen Häntsch, ..., Gerold A. Schneider, Manfred Eich, Alexander Y. Petrov

Correspondence

manohar.chirumamilla@tuhh.de

In brief

Chirumamilla et al. report a robust 2D photonic crystal emitter for thermophotovoltaic energy harvesting that remains structurally stable at 1,400°C, endures 6 months at 1,050°C, and survives hundreds of thermal cycles. Achieving 52% spectral efficiency, this cost-effective, scalable emitter enables reliable energy harvesting under extreme temperatures and harsh environments.

Chirumamilla et al., 2025, Cell Reports Physical Science 6, 102850
October 15, 2025
https://doi.org/10.1016/j.xcrp.2025.102850

CellPress

Cell Reports
Physical Science

CellPress
OPEN ACCESS

Article

2D photonic crystal emitter at 1,400°C for thermophotovoltaic energy harvesting

Manohar Chirumamilla,[1,2,9,*] Gnanavel V. Krishnamurthy,[3] Yen Häntsch,[4] Maik Finsel,[5] Guoliang Shang,[1] Surya S. Rout,[6,7,8] Lukas Maiwald,[1] Tobias Krekeler,[6] Martin Ritter,[6] Michael Störmer,[3] Kjeld Pedersen,[2] Tobias Vossmeyer,[5] Gerold A. Schneider,[4] Manfred Eich,[1,3] and Alexander Y. Petrov[1,3]

[1]Institute of Optical and Electronic Materials, Hamburg University of Technology, Eissendorfer Strasse 38, 21073 Hamburg, Germany
[2]Department of Materials and Production, Aalborg University, Fibigerstræde 16, 9220 Aalborg, Denmark
[3]Institute of Functional Materials for Sustainability, Helmholtz-Zentrum Hereon, Max-Planck-Strasse 1, 21502 Geesthacht, Germany
[4]Institute of Advanced Ceramics, Hamburg University of Technology, Denickestrasse 15, 21073 Hamburg, Germany
[5]Institute of Physical Chemistry, University of Hamburg, Grindelallee 117, 20146 Hamburg, Germany
[6]Electron Microscopy Unit, Hamburg University of Technology, Eissendorfer Strasse 42, 21073 Hamburg, Germany
[7]School of Earth & Planetary Sciences, National Institute of Science Education and Research, Jatani, Khurda 752050, India
[8]Homi Bhabha National Institute, Training School Complex, Anushaktinagar, Mumbai 400094, India
[9]Lead contact
*Correspondence: manohar.chirumamilla@tuhh.de
https://doi.org/10.1016/j.xcrp.2025.102850

SUMMARY

Spectrally selective emitters that endure extreme temperatures (exceeding 1,000°C) are vital for thermophotovoltaic energy harvesting. Here, we report a 2D photonic crystal emitter composed of yttria-stabilized zirconia particles on a tungsten mirror, fabricated through a simple and scalable self-assembly process. The emitter demonstrates spectral stability for 2 h and structural stability for 14 h at 1,400°C under high vacuum, with degradation attributed to zirconium nitridation, which is avoided under Ar or forming gas atmospheres. Long-term durability is demonstrated over 6 months and 200 thermal cycles at 1,050°C, effectively mitigating tungsten oxidation. The emitter achieves 52% spectral efficiency for a 0.72 eV photovoltaic band gap. This work offers perspectives on designing and implementing spectrally selective emitters that remain stable at high temperatures and resilient in harsh environments, representing a significant step forward in developing robust thermophotovoltaic energy-harvesting systems.

INTRODUCTION

Thermophotovoltaics (TPV) provides an excellent route to the conversion of thermal energy into electricity and can potentially be used for compact electricity generators and energy storage, providing on-demand energy retrieval in grid-scale thermal batteries.[1–10] A TPV cell directly converts thermal photons emitted from a hot surface into electrical power using a photovoltaic (PV) cell. The significant characteristics of TPV are small form factors (even at chip scale),[11–15] silent operation, and low maintenance. These features make it ideal for powering portable devices, for example in remote locations, humanitarian missions, and healthcare drones, by generating heat in micro-combustors[16] that utilize hydrocarbon fuels with high calorific values.[17] TPV can also be used for thermal batteries[2,18] that store heat energy from excessive renewable electricity sources and supply the necessary load to the electric grid during peak demand times. The main advantage of TPV in this case is the high conversion efficiency, which currently reaches up to 44%[10,19] and can be further increased by better spectral selectivity to approach the Carnot efficiency limit.[19] In this respect, TPV systems outperform thermoelectric generators (limited by 6% efficiency)[20,21] and reach the efficiencies of a typical gas power plant.

The radiative power of a blackbody is proportional to T^4, according to the Stefan-Boltzmann law, whereas the Wien displacement law states that the emitted radiation by a blackbody reaches its maximum at a wavelength proportional to $1/T$.[22,23] Therefore, higher operating temperatures in TPV systems offer the potential for larger radiative power and shift the blackbody maxima toward shorter wavelengths, which enable the utilization of highly efficient wide-band-gap PV cells with large open-circuit voltages, such as GaSb, GaAs, and Si.[24,25] Thermal radiation from a blackbody spans a broad spectral range, with most of it in the long-wavelength infrared region. These low-energy/out-of-band photons ($E < E_g$) cannot generate electron-hole pairs in the PV cell, leading to increased cell temperature and reduced efficiency. However, recent advancements in broadband reflective mirrors and front surface filters enable the redirection of these low-energy photons back to the emitter, significantly improving overall efficiency.[19,26,27] These innovations have achieved practical efficiencies of up to 44% at an emitter temperature of ~1,400°C.[10] Therefore, maintaining such high temperatures in a TPV system is essential to obtain high efficiencies. However, residual absorptivity in spectral control elements reduces efficiency. For instance, a 5% loss in broadband mirror reflectivity might lead to a 10% drop in system efficiency.[28,29]

An alternative way to achieve high conversion efficiency while simultaneously limiting low-energy photons is through spectral shaping,[30] which employs spectrally selective emitters.[7,8,31–41] Ideal spectrally selective emitters provide unitary and zero emissivities above and below the band gap of the PV cell, respectively. In addition to efficiently reducing the emission of out-of-band photons, these emitters should be designed to withstand high temperatures and repeated thermal cycling.[42,43] The state-of-the-art spectrally selective emitters face challenges with thermal stability beyond 1,000°C, leading to structural/spectral degradation.[8,38,44–46] Their long-term stability and ability to endure high temperatures over multiple cycles remain uncertain and require further investigation. Moreover, nanofabrication of spectrally selective emitters often relies on expensive and time-consuming top-down techniques such as electron/focused-ion beam lithography or reactive-ion etching.[39,47,48] These drawbacks form the cornerstone challenges for developing spectrally selective TPV energy-harvesting systems for industrial applications.

Here, we propose an innovative method to design spectrally selective emitters capable of functioning under high temperatures of up to 1,400°C and technical vacuum conditions of 2×10^{-2} mbar or under forming gas environments. A 2D photonic crystal (PhC)-based spectrally selective emitter, composed of a monolayer of yttria-stabilized zirconia (YSZ) particles and W-HfO_2 substrate, is fabricated using large-area nanofabrication techniques, magnetron sputtering, and self-assembly processes. The concept is based on our previous work with a ZrO_2 particle-based 2D-PhC emitter, which had limited thermal stability due to phase transformations of ZrO_2.[49] The YSZ-based 2D PhC emitter is designed to obtain spectral selectivity, which is tailored to match the external quantum efficiency spectrum of the GaSb PV cell with 0.72 eV band gap. However, at high temperatures, the efficiency is anticipated to decrease due to increased electron-phonon collision frequency. The presented 2D PhC emitter exhibits thermal stability at 1,400°C, and optical measurements indicate a high spectral conversion efficiency of up to 52% at 1,400°C. Further, the long-term thermal stability of the emitter is demonstrated through 6 months (4,320 h) of thermal annealing at 1,050°C and thermal endurance of up to 200 cycles under a forming gas environment, exhibiting remarkable structural durability and spectral selectivity. This is the highest reported temperature with long-term thermal stability and endurance for a spectrally selective emitter to date. The combination of high working temperature, thermal endurance, and a scalable, cost-effective, lithography-free fabrication process advances the development of stable spectrally selective emitters and promotes the broader adaption of TPV energy-harvesting systems.

RESULTS AND DISCUSSION

Spectrally selective band-edge emitter

A schematic presentation of the 2D PhC-based spectrally selective emitter is shown in Figure 1A. The PhC emitter consists of a monolayer of hexagonal close-packed (hcp) YSZ ceramic particles of 980 nm diameter on a W/HfO_2 structure, which is coated onto a single-crystalline Al_2O_3 substrate with [1–102] orientation. Oxide ceramic particles are prone to excessive grain growth and phase transformations at high temperatures, leading to irreversible structural damage. ZrO_2 particles, doped with 7.5 mol % yttrium have been chosen for their unprecedented thermal stability and capability of withstanding temperatures up to 1,500°C.[50] The W and HfO_2 film thicknesses were 200 nm and 20 nm, respectively. The 200-nm-thick W film completely blocks the transmission of light due to the significantly smaller penetration depth of optical fields in W.[51] Meanwhile, the 20 nm HfO_2 film exhibits a negligible impact on the optical properties of the PhC emitter and functions as a protective layer, preventing the oxidization of W. YSZ particles, as synthesized in Leib et al.,[50] with a standard deviation of <6%, are deposited onto the W-HfO_2 layer using a self-assembly process at the air-water interface.[52] The parameters for the YSZ particles were adopted from our previous work,[49] where particles with a 980 nm diameter demonstrated optimal spectral selectivity. YSZ particles support multiple Mie resonances, including quadrupole, hexapole, and octupole modes, which achieve critical coupling and near-perfect absorptivity.[49] The quadrupole resonance appears at 1.56 μm and marks the onset of a high absorption/emissivity region. The dipole mode is weakly interactive with tungsten substrate and reflected without significant absorption. Higher-order modes extend toward the 1 μm spectral range, although these are highly sensitive to both the substrate and the spatial arrangement of nanoparticles in the monolayer. Modifying the particle radius allows tuning of the spectral response: increasing the particle size shifts the cutoff wavelength defined by the quadrupole mode toward longer wavelengths, while decreasing it moves the cutoff toward shorter wavelengths. This tunability is particularly useful for aligning the absorption band edge with the external quantum efficiency of the PV cell. The YSZ-particle-based PhC structure is similar to a 2D PhC approach with hollow cavities in structured tungsten,[41] where we substitute the hollow cavities with ceramic resonators on unstructured tungsten.

A top-view scanning electron microscopy (SEM) image of the 2D PhC structure is shown in Figure 1C, which clearly exhibits a uniform distribution of YSZ particles over the W/HfO_2 layer. The inset presents a closely packed arrangement of YSZ particles forming an hcp lattice. A side-view image of the 2D PhC structure is shown in the inset of Figure 1B. A cross-sectional SEM image of the structure, obtained through a focused-ion beam (FIB) milling, is shown in Figure 1D and the supplemental information (Video S1 and Figures S1–S3). A scanning transmission electron microscopy (STEM) cross-sectional image of the emitter and the corresponding elemental mappings/spectrum images created by energy-dispersive X-ray spectroscopy (EDS) are shown in Figures 1E–1J and S4. The spectrum images reveal the presence of Y, Zr, W, Hf, and O within their respective layers. Figures 1F and 1G distinctly display a prominent concentration of Y and a comparatively lower concentration of Zr at the center of the particle, with bright and contrasting dark regions, respectively, as further illustrated in Figure S4A. For the rest of the particle, both the elements are uniformly distributed. As already hypothesized in our earlier study,[50] this finding reveals that during the synthesis of the YSZ particles, nucleation is predominantly initiated by the hydrolysis and polymerization of the more reactive yttria precursor (yttrium iso-propoxide). Thereafter, the growth phase involves hydrolysis and polymerization of both the yttria

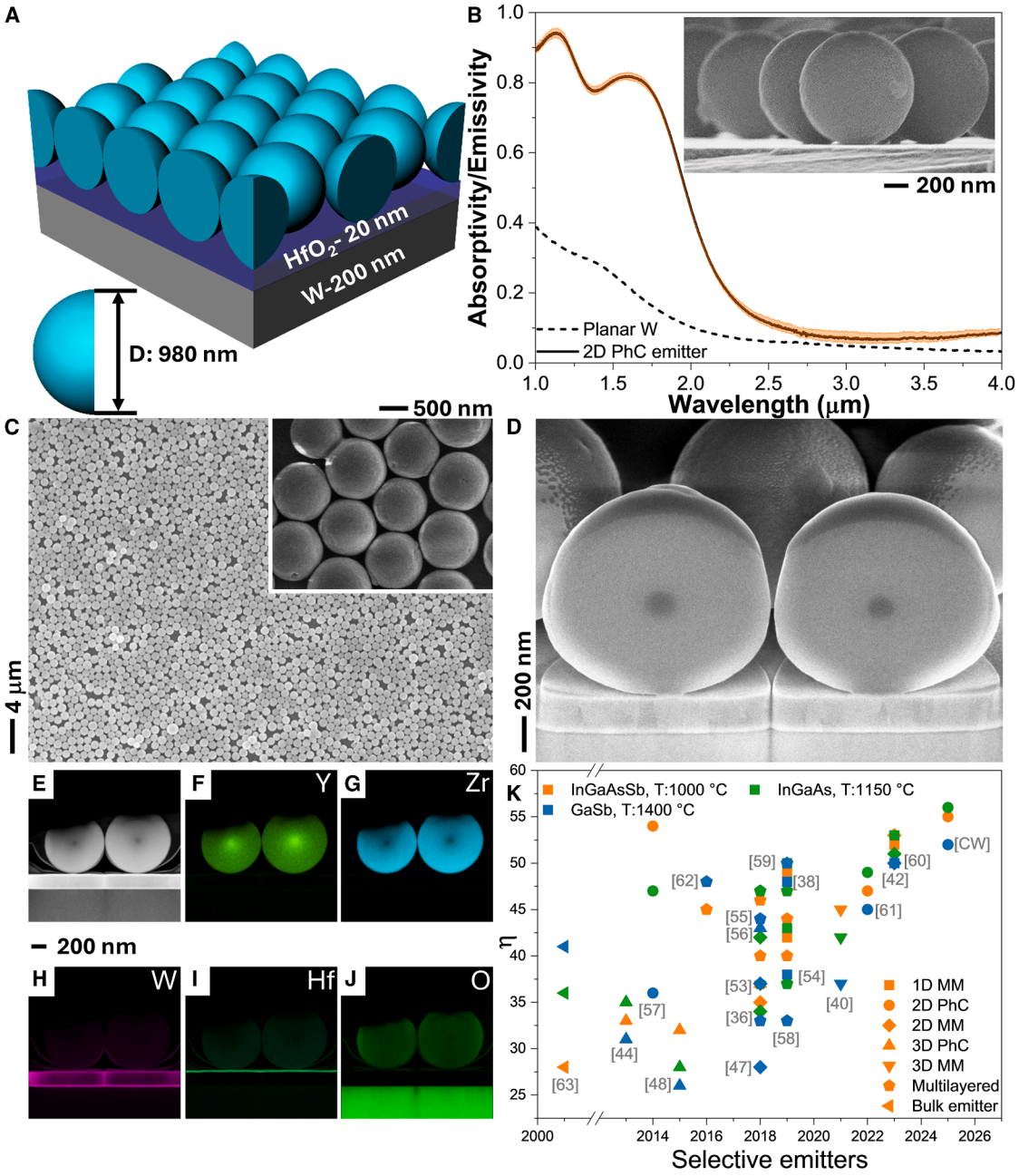

Figure 1. Design and experimentally realized 2D YSZ-based PhC emitter structure

(A) Schematic presentation of the 2D YSZ-based PhC emitter structure. The Al_2O_3 substrate is not shown in the illustration.

(B) Measured absorptivity/emissivity spectra of the 2D PhC emitter and a planar W structure. The inset shows the side-view SEM image of the 2D PhC emitter.

(C) Top-view SEM image of the 2D PhC structure, with inset showing a magnified view of an hcp arrangement of the YSZ particles.

(D) Cross-sectional SEM image of the structure.

(E) High-angle annular dark-field scanning transmission electron microscopy (HAADF-STEM) image of the cross-sectional lamella prepared from two YSZ particles.

(F–J) Elemental maps of (F) Y (K_α), (G) Zr (K_α), (H) W (M_α), (I) Hf (M_α), and (J) O (K_α) of the 2D PhC emitter.

(K) Calculated spectral efficiency η of the various selective emitters and a bulk emitter[36,38,40,42,44,47,48,53–63] for PV cells of InGaAsSb (0.55 eV), InGaAs (0.6 eV), and GaSb (0.72 eV) at respective operating temperatures of 1,000°C, 1,150°C and 1,400°C, such that the wavelength of blackbody maximal emission approximately coincides with the band-gap energy. Reference numbers are in brackets, with CW indicating current work.

precursor and the zirconia precursor (zirconium *n*-propoxide), leading to the formation of a core-shell-like structure.

Figure 1B shows the absorptivity/emissivity (α/ε) spectrum of the as-fabricated 2D PhC emitter at room temperature (RT). For reference, the α/ε spectrum of the W-planar structure (of 200 nm thickness) is included. Figure S5 displays the reflectivity spectra of W, W-HfO_2, and 2D PhC structures, clearly showing the absorption mechanism of the 2D PhC structure. The 2D PhC emitter reveals a step-function-like spectral selectivity, which is tailored to the absorption edge of the GaSb PV cell with a cutoff wavelength, λ_C, around 1.7 μm. The absorption edge is adjusted by the particle size.[49] The emitter exhibits high and low α/ε below and above λ_C, respectively, with a sharp decline around the λ_C, leading to below 5% α/ε at longer wavelengths. According to Kirchhoff's law of thermal radiation,[64,65] the emissivity of a hot radiating body equals its absorptivity at the same temperature. Thus, by measuring the absorptivity of the 2D PhC emitter at RT, the corresponding TPV-relevant spectral emissivity can be assessed. At elevated temperatures, the α/ε will change slightly due to the increasing electron collision frequency of tungsten.[51] The emitter exhibits under 5% variation in the spectral selectivity for the measurements taken at various spatial locations of the emitter, using a 0.5 μm light spot over a 2 cm^2 sample area. This indicates a uniform 2D PhC structure throughout the substrate, resulting from the homogenous deposition of the 2D YSZ-particle monolayer. Figure 1K shows the spectral efficiency η of various state-of-the-art spectrally selective emitters based on 1D–3D PhCs, metamaterials, and multilayered structures,[36,38,40,42,44,47,48,53–62] as well as a bulk emitter,[63] calculated using Equation 1[25] for InGaAsSb, InGaAs, and GaSb PV cells, where the efficiencies are shown at their respective operating temperatures of 1,000, 1,150°C and 1,400°C, owing to the cutoff wavelengths.

The spectral efficiency is given by

$$\eta = \int_{E_g}^{\infty} \frac{E_g}{E} \varepsilon(E) I_{BB}(E,T) dE \Big/ \int_{0}^{\infty} \varepsilon(E) I_{BB}(E,T) dE, \quad \text{(Equation 1)}$$

where E and I_{BB} correspond to the incident thermal photon energy and blackbody spectral power density at the emitter temperature, respectively. η defines the ratio of the convertible thermal radiation energy by the PV cell to the total radiated thermal energy by the emitter. For a photon possessing $E > E_g$, the excess energy is dissipated via thermalization. Consequently, the remaining fraction of energy that is transformed into electricity is $\frac{E_g}{E}$. Note that the TPV system efficiency is smaller than the spectral efficiency, as it includes other factors such as quantum efficiency, fill factor of PV cell, and thermal isolation of the emitter.[7] Furthermore, electron-phonon scattering at elevated temperatures also contributes to efficiency losses.[51] η is calculated based on the RT optical properties of the emitter, so an estimated reduction in efficiency of up to 6% can be expected, primarily due to increased emissivity at longer wavelengths resulting from increasing electron-phonon collision frequency. Among different structural geometries for selective emission, 1D metamaterials and 2D PhC structures demonstrate the highest η owing their low emissivity at longer wavelengths.

Although bulk emitters, such as NiO-doped MgO, exhibit excellent thermal stability under ambient atmosphere, they have non-tunable spectral response and can have detrimental long-wavelength emission.[63] Nanostructured materials with 2D and 3D architectures often feature sharp nanoscale edges, which are particularly vulnerable to surface diffusion at elevated temperatures. For evaluation of the thermal stability of emitters, the retention of their spectral properties is considered as a key indicator. Since surface diffusion tends to follow the gradient of edge curvature,[66] structures with pronounced edges are more prone to morphological degradation. Therefore, it is advantageous to utilize emitters without sharp edges such as planar thin-film architectures, e.g., 1D layered metamaterials and Fabry-Pérot resonators, or 2D PhC with ceramic nanoparticles. However, as shown elsewhere, tungsten oxidation makes metamaterials with alternating thin metal layers (~20 nm) susceptible to spectral degradation under high temperatures and extended heating periods.[33,42] In contrast, 2D PhC structures, with their thicker W layer, are less sensitive to oxidation of the upper W surface and offer better spectral stability under such conditions, making them more suitable for extended high-temperature applications. Also, the YSZ-particle-based 2D PhC outperforms other state-of-the-art spectrally selective emitters due to its step-like sharp-edge spectral characteristics, as seen in Figure 1K. It should be noted that the spectral efficiencies were calculated using Equation 1 and emissivity spectra presented in the referenced publications. As a result, the data calculated and presented in Figure 1K may differ from those published in the original studies.

Spectral stability of the 2D PhC emitter at high temperatures

The α/ε spectra of the 2D PhC emitter, taken at RT, before and after annealing at 1,400°C under vacuum pressure (normal air environment outside the vacuum chamber) of 2×10^{-6} mbar over various durations, extending up to 14 h, are shown in Figure 2A. The calculated α/ε spectrum of the emitter, shown as a dotted trace in Figures 2A and S6, demonstrates reasonable agreement with the measured spectra. After annealing at 1,400°C for 1 h, the 2D PhC emitter structure exhibits a step-function-like spectral characteristic, similar to that of the original as-fabricated structure. This is accompanied by an enhancement in the peak intensity around 1.7 μm due to thermally induced structural modifications such as grain growth in the structure. Furthermore, a decrease in α/ε in the mid-infrared regions is noticed, wherein the change in the electron collision frequency of the W, owing to grain growth, improves metallic reflection.[51] When the emitter is annealed for 2 h at 1,400°C, no further significant change in the spectral selectivity is observed. Yet, after 6 h and 10 h of thermal annealing at 1,400°C, a slight increment in the α/ε in the mid-infrared regions can be observed. A significant rise in the α/ε within the mid-infrared region is noticeable after 14 h of annealing at 1,400°C.

Spectral efficiency η of the 2D PhC emitter

Figure 2B presents the spectral energy density of the 2D PhC emitter, the blackbody radiator, and W planar emitter at

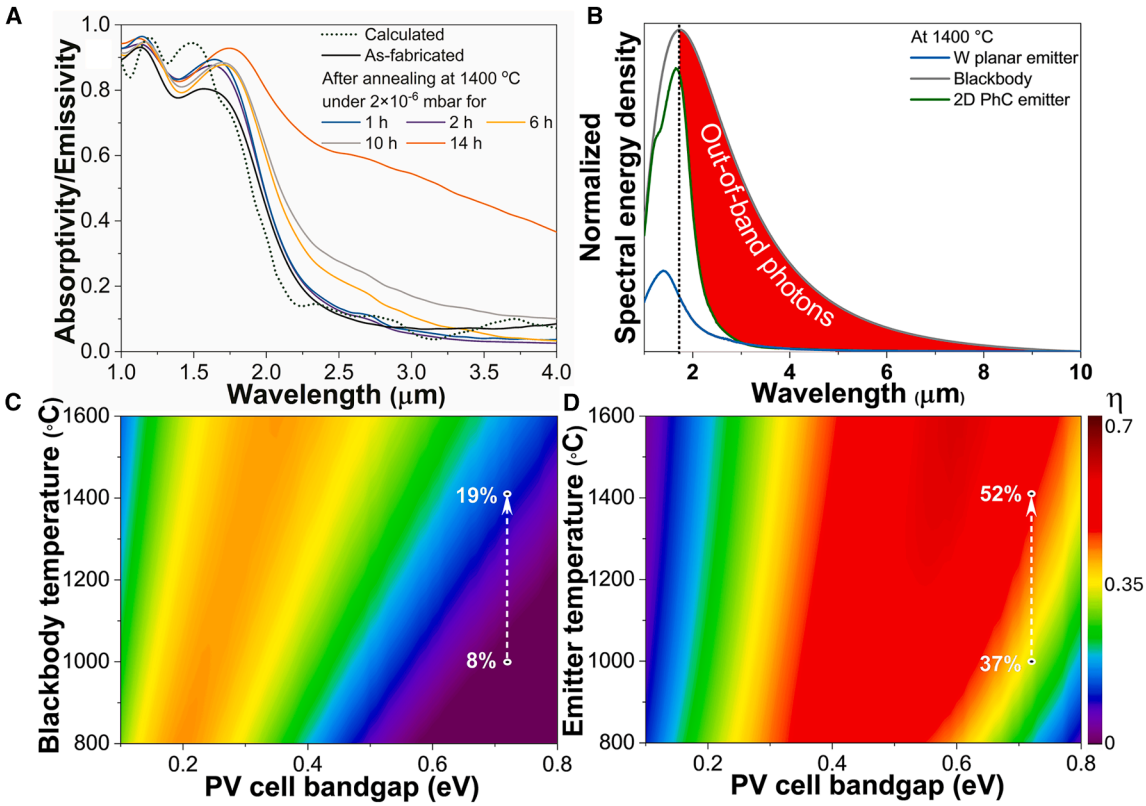

Figure 2. Thermal stability at 1,400°C and spectral efficiency

(A) Measured α/ε spectra of the emitter at RT, as fabricated and after annealing at 1,400°C for various annealing durations, 1 h–14 h, under vacuum pressure of 2×10^{-6} mbar. The dotted trace shows the calculated spectrum of the emitter using CST MW simulation.

(B) Normalized spectral energy density of a blackbody emitter, 2D PhC emitter, and W emitter operating at 1,400°C. The dotted line shows the λ_C of GaSb PV cell and the normalized spectral energy above λ_C due to out-of-band photons.

(C and D) Contour maps showing the η of a TPV cell versus emitter temperature and PV cell band gap for (C) blackbody and (D) 2D PhC emitter.

1,400°C, normalized to the blackbody maxima at 1,400°C. The spectral energy density of both the 2D PhC emitter and W emitter are obtained from the experimental α/ε spectra. The blackbody radiator shows a maximum radiance in the near-infrared region and a wide energy tail (shown by a red-shaded area) in the mid-infrared region, whereas the W planar emitter exhibits low spectral energy densities below the λ_C. Given that W is a refractory metal with lossy dielectric properties below 900 nm and lossy metal properties in the near-infrared region,[51] the W planar structure exhibits strong reflection below 1.7 μm wavelength. Therefore, only a small percentage of energy is radiated by the W emitter below the λ_C, thereby reducing the current generated in a PV cell. η of a blackbody radiator and 2D PhC emitter as a function of the temperature T and PV cell band-gap energy E_g is shown in Figures 2C and 2D, respectively, calculated using Equation 1. When the TPV system operates at 1,400°C with a PV cell band gap of 0.72 eV, the blackbody exhibits η of 19%. The η drops to 8% when the operating temperature decreases to 1,000°C. The observed low η is due to the high spectral emittance beyond λ_C, whereas the 2D PhC emitter exhibits a spectral efficiency of 52% when operating at 1,400°C for the same PV cell, which is around 2.7-fold higher than that of a blackbody. At 1,000°C, the efficiency declines to 37%, which is around 4.6-fold higher than that of the blackbody. Thus, the 2D PhC emitter shows a substantial enhancement in η, attributed to its step-function-like spectral selectivity. As shown in the red-shaded area of Figure 2B, the 2D PhC emitter significantly reduces the emission of out-of-band photons into free space. It also effectively minimizes mid-infrared photon absorption within the PV cell housing, eliminating the need for front surface filters or reflective mirrors behind the PV cell. Figure S7 illustrates that η increases with a rise in temperature for a given band gap of 0.72 eV. Consequently, higher operating temperatures combined with wide-band-gap PV cells of large open-circuit voltages result in high η.[22,25]

Structural investigation of the 2D PhC emitter

When evaluating the annealing behavior of nanostructures at elevated temperatures, it is essential to consider both short-duration exposure at high temperatures and prolonged exposure at lower temperatures.[67] Short-term high-temperature annealing helps assess immediate structural responses such as phase transformations, grain growth, and robustness against thermal stresses, whereas prolonged annealing at lower temperatures provides critical insights into long-term stability and degradation mechanisms.

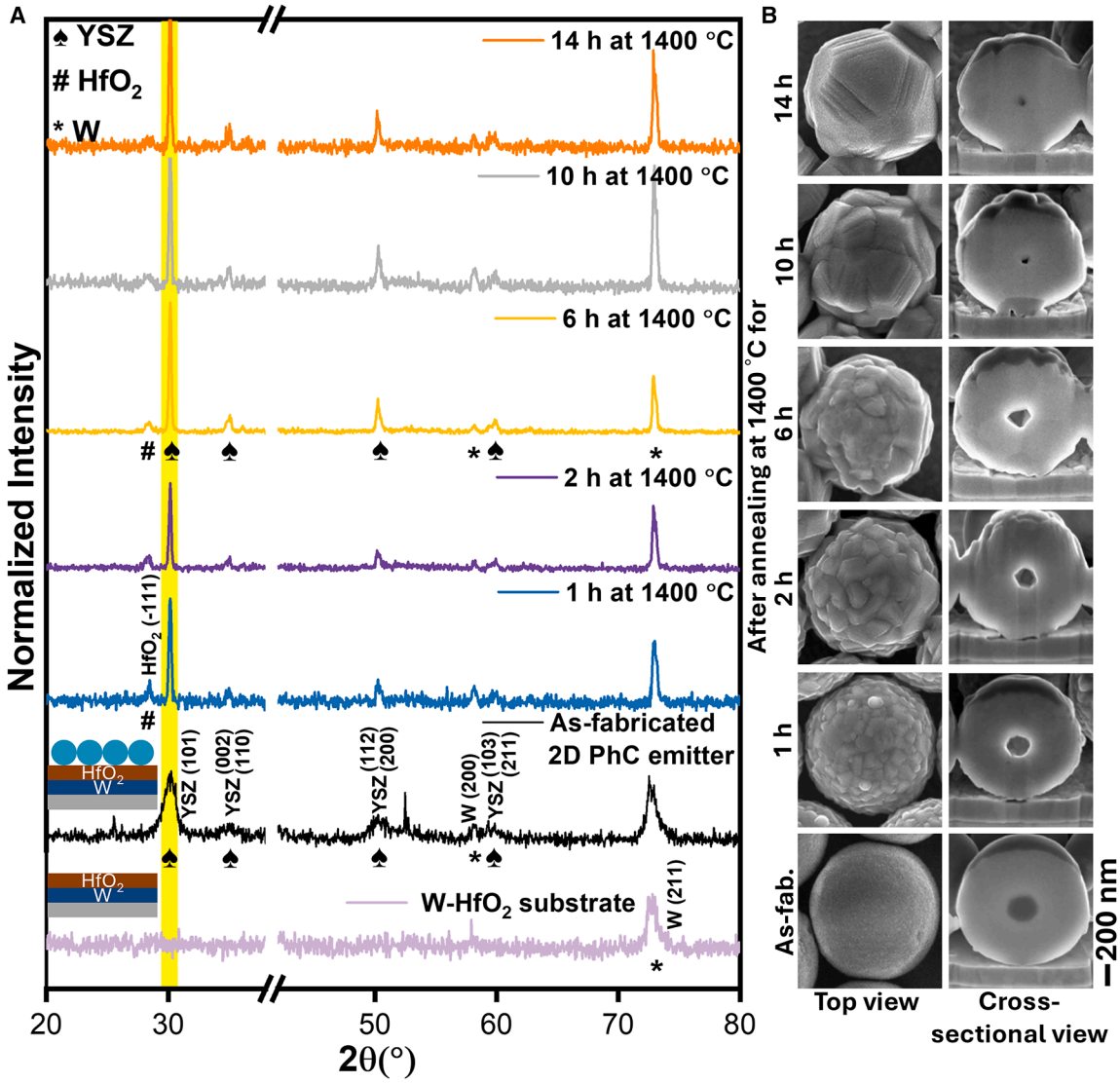

Figure 3. Structural stability of the emitter after annealing at 1,400°C

(A) XRD patterns of the 2D PhC emitter for as-fabricated and after annealing at 1,400°C under vacuum pressure of 2×10^{-6} mbar, taken at RT for various thermal annealing durations ranging from 1 h to 14 h.

(B) The corresponding top-view (left column) and cross-sectional (right column) SEM images of the YSZ particles showing the structural evolution due to grain growth in the YSZ particle. Scale bar, 200 nm.

Ex situ X-ray diffraction (XRD) measurements of 2D PhC structure taken at RT, as-fabricated and after annealing at 1,400°C, for various thermal annealing durations under a vacuum pressure of 2×10^{-6} mbar, are shown in Figure 3A. Top-view and cross-sectional SEM images of the YSZ particles after thermal treatment are shown in Figure 3B (see also Figures S8 and S9; Videos S2 and S3), illustrating the grain-growth-related evolution in YSZ particles as duration of thermal annealing increases. For comparison, the diffraction pattern of a W-HfO_2 structure (without YSZ particles) is also presented in Figure 3A, where the (211) plane at 2θ = 73.2° and (110) at 2θ = 40.3° are clearly seen (Figure S10), which correspond to the body-centered cubic (BCC) phase of α-W (JCPDS 00-004-0806). The α-phase W is thermodynamically stable,[68] and the metastable β-phase W is not observed in the as-fabricated film. The 20 nm HfO_2 film, on top of the 200 nm W layer, is not clearly resolved in the XRD pattern. The as-fabricated 2D PhC emitter structure reveals a strong (101) reflex at $2\theta = 30.3°$ (Figure 3) and other weak reflexes of the tetragonal YSZ phase ((112), (200) at ~50°; (103), (211) at ~60°; PDF #00-042-1164 and PDF #01-079-1763),[69,70] in addition to the W reflexes. As seen in Figure 3B, a smooth surface of the YSZ particle is observed for the as-fabricated emitter. The enlarged SEM images are shown in Figures S8A and S9A. After subjecting the structure to 1,400°C for 1 h, SEM images in Figures 3B, S8B, and S11E reveal YSZ particles forming tiny grains due to thermal annealing. This subsequently leads to the

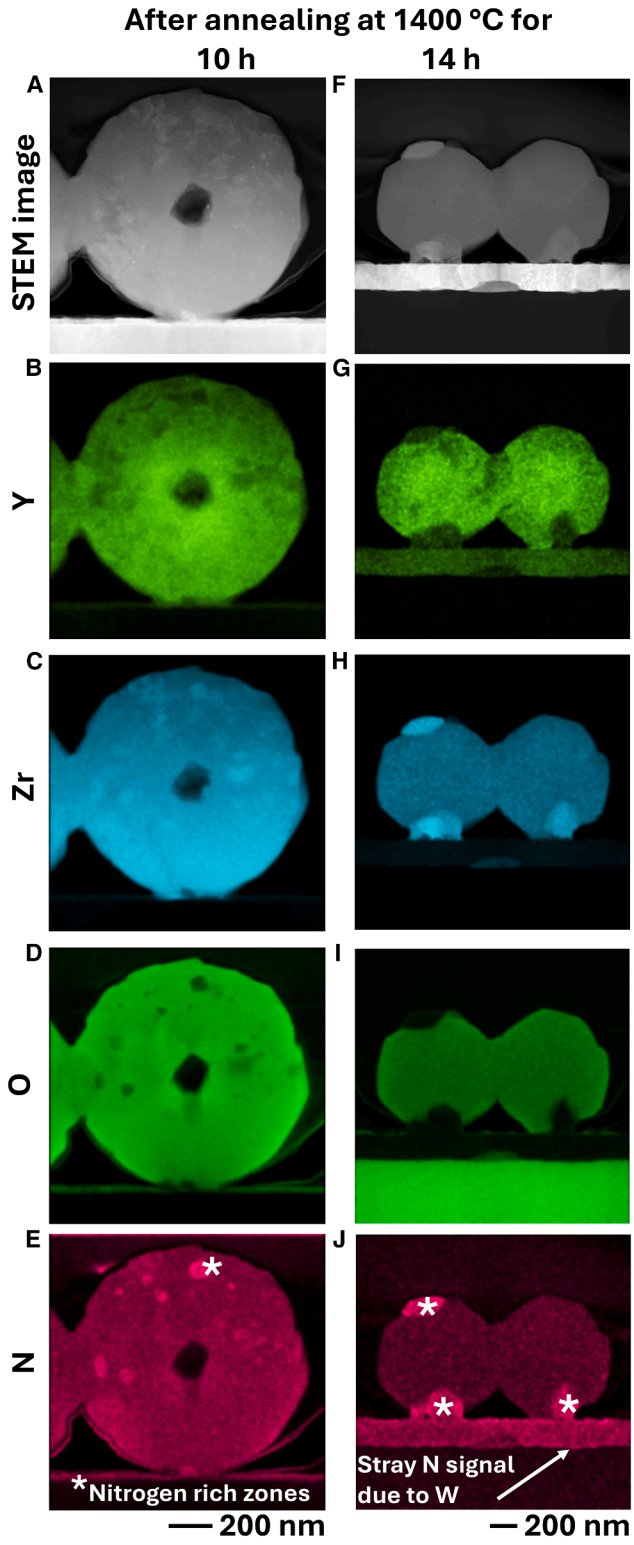

Figure 4. Elemental analyses of the emitter after annealing at 1,400°C for 10 h and 14 h

HAADF-STEM image of the emitter annealed at 10 h (A) and 14 h (F) at 1,400°C, respectively, and the corresponding spectrum images (B and G, C and H, D and I, and E and J) showing the distribution of Y, Zr, O, and N. Scale bar, 200 nm.

narrowing of the YSZ (101) reflex in the XRD pattern. Furthermore, the Y-rich core, initially observed at the center of the particle, has diffused throughout the particle, creating a hollow core, as shown in Figures 3B and S11E. Despite the formation of a hollow core, the 2D PhC emitter retains the same spectral selectivity as the original structure (Figure 2A). Upon heating, the W reflex (211) narrows as a result of the grain growth in W (Figure S12). Additionally, the reflex (−111) at $2\theta = 28.3°$, corresponding to monoclinic HfO_2 (JCPDS 034-0104), becomes distinct due to the grain growth in HfO_2.

After annealing the emitter for durations ranging from 2 h to 14 h at 1,400°C, the structural phases of YSZ and W remain unchanged. Nonetheless, grain growth is clearly noticeable (Figures 3B, S8, and S9). The STEM image in Figure 4A and SEM image in Figure S12 reveal that the emitter structure remains stable even after a 10 h of annealing at 1,400°C. On the other hand, Figure 4E emphasizes the zones rich in N (marked with an asterisk) within the YSZ particle, while the same zones in Figure 4D show a lack of O content, indicating O deficiency. Under a vacuum pressure of 2×10^{-6} mbar, the N_2 partial pressure stands at 1.5×10^{-6} mbar. It is known from the literature[71] that O vacancies are generated by substituting Y in the ZrO_2 matrix to maintain electroneutrality. Elevated temperatures above 1,400°C facilitate a gradual diffusion of N from the atmosphere and filling of the O vacancies in the ZrO_2 matrix, forming N-rich zones within the YSZ particle. However, Zr remains present in these N-rich areas (Figure 4C). Additionally, after annealing the emitter for 14 h at 1,400°C, the YSZ particle displays prominently developed crystal facets (Figures 3B and S8F) with excellent structural stability. While the hollow core of the YSZ particle remains, it diminishes in size due to the grain growth. A STEM image in Figure 4F illustrates the structural integrity after heat treatment, showcasing the W thin film and YSZ particles. Yet, akin to the sample annealed for 10 h, zones rich in N (as seen in Figure 4J and the corresponding O-deficient zones in Figures 4I and S13 for magnified images) become apparent after 14 h of annealing at 1,400°C. The spatial overlapping of Zr and N elements strongly indicates the formation of ZrN particulates within the YSZ particle. Given that ZrN is a refractory metal,[72] its interaction with light might introduce additional losses, explaining the increase in α/ε in the mid-infrared region (Figure 2A) after annealing the emitter for 14 h at 1,400°C. Spectral degradation after annealing for 14 h is linked to the vacuum environment and residual N interaction rather than the intrinsic instability (such as sublimation of the material, loss of the continuous thin film, groove formation at the grain boundaries, voids in the thin-film structure, and phase change[38,42,46,49,54,73,74]) of the 2D PhC structure and can be avoided by heating the emitter under Ar atmosphere.[39]

Thermal stability of the emitter at extreme operating conditions

To evaluate the impact of O_2 on the thermal resilience of the emitter, 2D PhC structures were annealed at 1,400°C for 1 h under different environmental conditions. The following annealing methods are used: (1) the emitter is subjected to heat treatment at a medium vacuum pressure of 2×10^{-2} mbar, with the heating chamber surrounded by ambient air; or (2) the emitter is heated

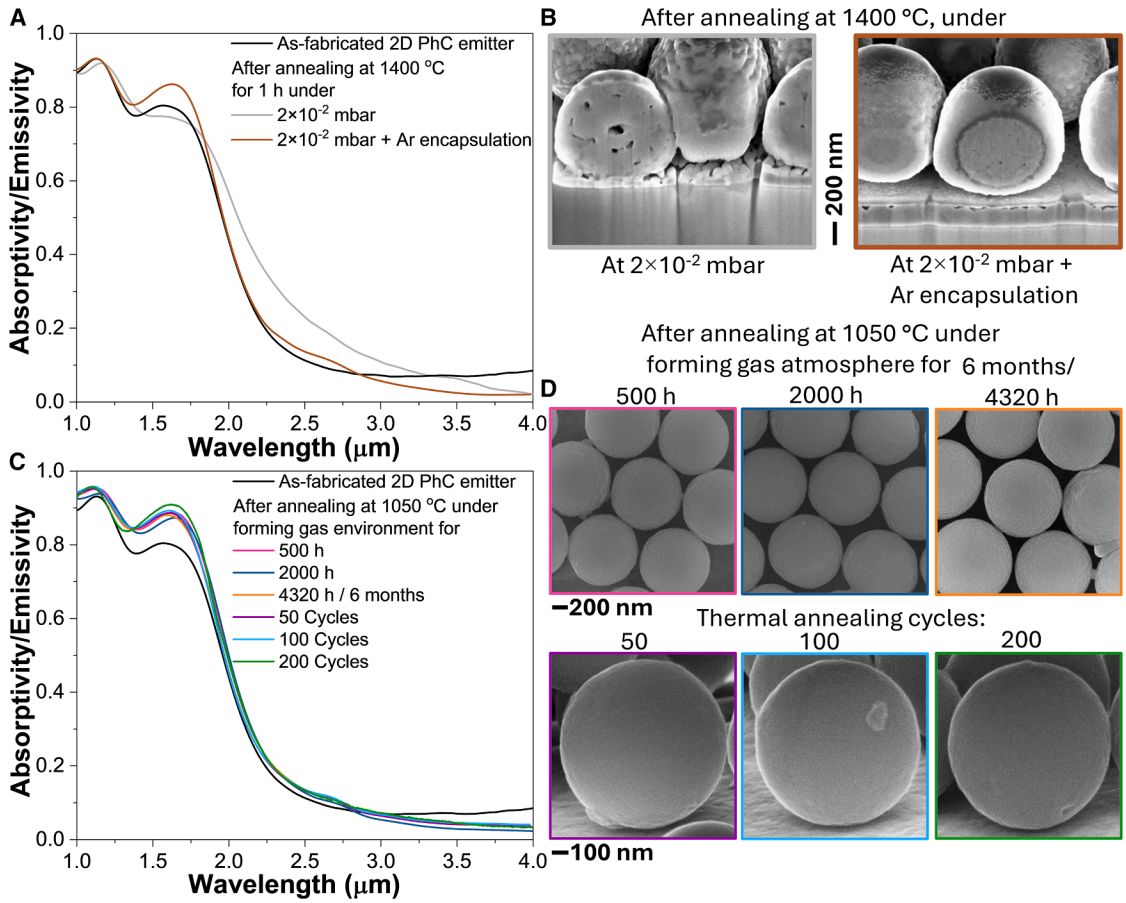

Figure 5. Long-term thermal stability and durability of the 2D PhC emitter

(A and B) (A) Experimental α/ε spectra of the *ex situ* annealed 2D PhC emitter structure before and after annealing at 1,400°C for 1 h under a medium vacuum pressure of 2×10^{-2} mbar, and encapsulation of the vacuum chamber with Ar atmosphere. The corresponding SEM images are shown in (B).

(C and D) (C) Experimental α/ε spectra of the *ex situ* annealed 2D PhC emitter at 1,050°C, under standard atmospheric pressure and forming gas environment. The corresponding SEM images are shown in (D).

similarly to (1) but with the ambient air replaced by Ar gas to reduce the partial O_2 pressure inside the vacuum chamber (schematics are presented in Figure S14). Figure 5A shows the α/ε spectra of the 2D PhC emitter, comparing the as-fabricated state and post-annealing state at 1,400°C under the aforementioned conditions. A noticeable increase in the α/ε beyond the λ_C is observed when the emitter is heated, as described in case (1). The cross-sectional SEM image shown in Figure 5B reveals a reduction in the thickness of the underlying W layer. Under a medium vacuum pressure of 2×10^{-2} mbar, where the partial O_2 pressure in the vacuum chamber is $\sim 2 \times 10^{-3}$ mbar, oxygen tends to infiltrate the structure and react with W, leading to the formation of WO_x.[38,39,51,73] Nonetheless, these WO_x compounds are highly volatile and tend to sublimate at elevated temperatures, leading to a reduction in the thickness of the W layer. In an earlier study, the formation of $WO_{2.9}$ and WO_2 was observed at temperatures above 1,000°C.[38] Despite this, the YSZ particles remain inert to reactions with O_2, ensuring that the Mie resonances of the dielectric particles below the λ_C remain consistent.

To prevent the structural degradation induced by O_2 under medium-vacuum conditions, the vacuum chamber was then surrounded by Ar (99.999%) gas, case (2), resulting in O_2 concentration reduction down to 17 ppm in the enclosed environment. When the 2D PhC emitter is heated under these conditions, the α/ε spectrum exhibits a slight variation, with the spectral selectivity remaining closely aligned with the as-fabricated structure. A cross-sectional SEM image in Figure 5B distinctly showcases that the W layer and the YSZ particles remain intact. As observed in the case of annealing under high vacuum, a hollow core also forms when the YSZ particle is annealed under medium-vacuum conditions with Ar encapsulation (Figures 5B and S15). The preservation of emitter structural integrity is likely due to the reduction of O_2 concentration levels in the surrounding environment achieved by the Ar encapsulation.

Long-term thermal stability and durability under cyclic thermal stress are critical for the operation of the TPV systems. Current state-of-the-art selective emitters have demonstrated thermal stability up to 500 h at 1,000°C[42,75,76] and can endure 50 thermal annealing cycles.[42] Key challenges in maintaining extended

thermal stability include surface diffusion, grain growth, oxidation, phase change, and recrystallization. To investigate the long-term thermal stability in the absence of oxidation, the 2D PhC emitter was tested at 1,050°C for up to 4,320 h (6 months) in forming gas (95% Ar and 5% H_2 with 99.999% purity) at standard atmospheric pressure. Figure 5C shows the α/ε spectra of the 2D PhC emitter at RT both before and after annealing at 1,050°C. After 500 h of annealing, the α/ε spectrum looks similar to the as-fabricated structure with a slight decrease in α/ε in the mid-infrared region, likely due to grain growth in W. The SEM image in Figure 5D confirms the intact structure of the emitter. After 2,000 h of thermal annealing, spectral selectivity remains unchanged. Similarly, after annealing for an extended duration of 4,320 h (6 months) at 1,050°C, no additional changes in the spectral selectivity or structural integrity are observed (Figures 5C and 5D). XRD patterns shown in Figure S16 reveal no new phase reflections in YSZ and W, confirming that the tetragonal phase of YSZ is intact and no WO_x has occurred, underlining the exceptional long-term thermal resilience of the 2D PhC emitter.

The thermal cyclic endurance of the 2D PhC emitter was evaluated by subjecting it to 1,050°C under standard atmospheric pressure in forming gas environment for 200 cycles. In each cycle, the emitter was heated from RT to 1,050°C, held at that temperature for 1 h, and cooled down to RT with a ramp rate of 10°C/min. After 50 cycles, as seen in Figure 5C, there is no change in the spectral selectivity compared to the as-fabricated structure observed. Likewise, after undergoing 100 and 200 thermal cycles, the α/ε spectra remained consistent with the as-fabricated structure. Figure 5D presents the corresponding SEM images of the YSZ particles and XRD spectra in Figure S17, showcasing their exceptional resilience to repeated thermal cycling and excellent structural stability.

To summarize, we have demonstrated the extended thermal stability of a 2D PhC structure, based on YSZ particles, as a spectrally selective emitter for TPV energy harvesting. By coupling the Mie resonances of the 980 nm YSZ particle with the W surface, the 2D PhC emitter is designed to match its spectral selectivity with the band gap of the GaSb PV cell at 0.72 eV. Spectral stability for 2 h is observed at a maximum temperature of the emitter of 1,400°C under high-vacuum conditions of 10^{-6} mbar. Beyond this duration, spectral degradation is observed owing to N diffusion and the subsequent formation of ZrN nanoparticulates. Nitridation can be inhibited by using surface passivation coatings or yttria-stabilized hafnia particles, and this will be the focus of future work. Moreover, 2D PhC structure exhibits structural stability after annealing at 1,400°C for 14 h under high-vacuum conditions of 10^{-6} mbar. Regardless of thermal annealing durations at 1,400°C, YSZ particles are highly stable and exhibit a tetragonal lattice structure. The thermal stability of the emitter was also tested under a rough vacuum environment of 10^{-2} mbar with varying partial pressure of O_2. By minimizing the partial O_2 pressure in the annealing chamber, it was demonstrated that the emitter again exhibits thermal stability at 1,400°C for 1 h.

Further, we demonstrated the long-term thermal stability of 2D PhC structures at 1,050°C in forming gas environments at standard pressure for a duration of 6 months and 200 thermal cycles, establishing these structures as ideal selective emitters for TPV energy-harvesting systems. The 2D PhC emitters can be combined with reflective PV cells to further improve spectral efficiency. The self-assembly approach used here is cost effective and scalable to large surface areas, making such emitters promising components for constructing efficient, industrial-scale systems, such as thermal batteries or waste heat recovery. We show that a forming gas environment can help to solve the W oxidation problem.

METHODS

2D PhC emitter fabrication

YSZ particles were synthesized following the sol-gel method described by Leib et al.[50] The sol-gel synthesis parameters described in Leib et al.[50] were modified to obtain YSZ particles with a 7.5 mol % yttrium content and an average diameter of 980 nm after calcination, including a reduction in the stabilizer concentration and an increase in water content. These adjustments resulted in a faster hydrolysis rate, leading to a shorter induction period and a smaller particle size of 980 nm (after calcination). Additionally, the stirring time was set to 40 s to minimize primary particle aggregation. The calcination process was conducted at 600°C for 3 h in a muffle furnace (L9/SKM, Nabertherm) under ambient atmosphere, with both heating and cooling rates set to 5°C/min.

For monolayer formation, the self-assembly process at the air-water interface was adapted from Vogel et al.[52] Sapphire substrates (5 × 5 mm) coated with a 200 nm W layer and a 20 nm HfO_2 layer were utilized to deposit the particle monolayer. Prior to deposition, the substrates were treated with oxygen plasma to produce a hydrophilic surface. The YSZ particles were suspended in ethanol and homogenized by sonication for 15 min, yielding a concentration of 1 g/L. The YSZ-particle suspension was then carefully dripped onto the surface of water in a crystallizing dish using a pipette until the water surface was completely covered with YSZ particles. Floating YSZ particles were observed as white domains at the air-water interface, and the addition was terminated once the water surface was entirely covered to avoid multilayer formation. The sapphire substrates with the W/HfO_2 coating were then submerged under the water and gently lifted at a 45° angle, successfully forming a monolayer of YSZ particles. The substrates were stored at RT under a shallow angle for drying.

Thermal annealing

Emitter structures were annealed in a high-temperature heating stage (Linkam, TS1500) at 2×10^{-2} mbar vacuum pressure using a rough vacuum pump, and in a high-temperature vacuum furnace (RD-G WEBB) at 2×10^{-6} mbar vacuum pressure. The temperature was ramped at a rate of 10°C min^{-1}. O_2 concentration in the encapsulated area was measured using an O^+ sensor (sensor type: SO-B0-010, in the range up to 2,000 ppm, purchased from SENSORE Electronic) and assembled on a generic sensor board. Ar gas (99.999% from Linde) was used to encapsulate the annealing chamber.

Reflection measurements

The diffuse reflection spectra of the emitter structures, for as-fabricated and after annealing at high temperatures, were

measured using a UV-visible, near-infrared spectrometer (PerkinElmer Lambda 1050) and a Fourier transform infrared spectrometer (FTIR-Vertex 70, Bruker) in the ranges of 0.3–2.5 μm and 1–10 μm, respectively. The optical absorptivity α is obtained by $\alpha = 1 - \rho - \tau$, where ρ and τ are diffuse reflectivity and transmissivity, respectively. Due to a 200-nm-thick bottom W layer, we realized $\tau = 0$ in the measured spectral range. Thus, absorptivity, $\alpha = 1 - \rho$, can be directly obtained from the reflection spectra.

Morphology and elemental analysis of the emitter structure

Cross-sectional STEM samples were prepared with a FIB (FEI Helios G3 UC) machine using a 30 keV gallium ion beam and transferred to Cu lift-out grids via the lift-out technique. The samples were sputtered with a 20 nm layer of Au before FIB preparation to prevent charging during FIB preparation. The final thickness of the lamellae was around 100 nm. An FEI Talos F200X transmission electron microscope equipped with a high-brightness Schottky-FEG (X-FEG) and a four-quadrant SDD-EDS system (solid angle of 0.9 srad) was used for high-angle annular dark-field (HAADF) imaging and EDS analysis. HAADF images were acquired with a take-off angle of 16–82 mrad. Bright-field STEM images were acquired with an objective aperture to enhance the contrast of individual grains. Spectrum images were obtained using a probe current of 1 nA and a dwell time of 5 μs per pixel. The resolution of the spectrum image is 1,024 × 1,024 pixels, 1.5 nm in size, resulting in a horizontal field of view of 1.56 μm. Velox 2.1 (FEI) was used for data acquisition and visualization. For spectral imaging, the energies of the following elements were used: Al-K_α (1.49 keV), O-K_α (0.52 keV), Hf-M_α (1.64 keV), Y-K_α (14.931 keV), Zr-K_α (15.744 keV) and W-M_α (1.77 keV).

XRD measurements

XRD measurements were conducted using a Bruker D8 advanced diffractometer. Cu K_α (λ = 0.15405 nm) radiation was used to investigate the emitter structure. The measurements were performed using parallel beam geometry. The diffraction patterns (2θ from 20° to 90°) were recorded with an increment of 0.04° and a step time of 16 s.

RESOURCE AVAILABILITY

Lead contact

Requests for further information and resources should be directed to and will be fulfilled by the lead contact, Prof. Manohar Chirumamilla (manohar.chirumamilla@tuhh.de).

Materials availability

This study did not generate any new unique materials.

Data and code availability

- All data are available in either the main text or supplemental information.
- No new code was utilized in conducting this study.
- Any additional information required to reanalyze the data reported in this paper is available from the lead contact upon request.

ACKNOWLEDGMENTS

The authors gratefully acknowledge financial support from the Deutsche Forschungsgemeinschaft – Projektnummer 192346071 – SFB 986. M.C. acknowledges financial support from the Danish Council for Independent Research (Danmarks Frie Forskningsfond [DFF], Tematisk forskning – Fri grøn forskning, contract no. 4307-00221B). Publishing fees supported by Funding Programme Open Access Publishing of Hamburg University of Technology (TUHH).

AUTHOR CONTRIBUTIONS

M.C., A.Y.P., and M.E. designed the experiments; G.V.K. and M.S. fabricated the W-HfO_2 structures, performed XRD measurements, and analyzed the diffraction patterns considering phase formation and structural properties; M.F. and T.V. synthesized the YSZ particles; Y.H., M.F., and G.A.S. deposited the YSZ particles onto the W-HfO_2 structure; M.C., G.S., and L.M. performed the CST simulations; M.C. and K.P. investigated the long-term thermal stability of the 2D PhC emitter; M.C. investigated the optical properties of the 2D PhC emitters; S.S.R., T.K., and M.R. performed the STEM imaging and elemental mapping; M.C., A.Y.P., and M.E. performed the analysis and then interpreted the data; M.C., A.Y.P., and M.E. supervised the project; and M.C. wrote the manuscript. All authors discussed the results of the manuscript and provided comments for its finalization.

DECLARATION OF INTERESTS

The authors declare no competing interests.

SUPPLEMENTAL INFORMATION

Supplemental information can be found online at https://doi.org/10.1016/j.xcrp.2025.102850.

A video abstract is available at https://doi.org/10.1016/j.xcrp.2025.102850#mmc5.

Received: December 11, 2024
Revised: May 18, 2025
Accepted: August 25, 2025
Published: September 24, 2025

REFERENCES

1. Amy, C., Seyf, H.R., Steiner, M.A., Friedman, D.J., and Henry, A. (2019). Thermal energy grid storage using multi-junction photovoltaics. Energy Environ. Sci. *12*, 334–343.
2. Datas, A., López-Ceballos, A., López, E., Ramos, A., and del Cañizo, C. (2022). Latent heat thermophotovoltaic batteries. Joule *6*, 418–443.
3. Dias, M.R.S., Gong, T., Duncan, M.A., Ness, S.C., McCormack, S.J., Leite, M.S., and Munday, J.N. (2023). Photonics roadmap for ultra-high-temperature thermophotovoltaics. Joule *7*, 2209–2227.
4. Sakakibara, R., Stelmakh, V., Chan, W.R., Geil, R.D., Krämer, S., Savas, T., Ghebrebrhan, M., Joannopoulos, J.D., Soljačić, M., and Čelanović, I. (2022). A high-performance, metallodielectric 2D photonic crystal for thermophotovoltaics. Sol. Energy Mater. Sol. Cell. *238*, 111536.
5. Song, J., Jang, J., Lim, M., Choi, M., Lee, J., and Lee, B.J. (2022). Thermophotovoltaic Energy Conversion in Far-to-Near-Field Transition Regime. ACS Photonics *9*, 1748–1756.
6. Lee, B., Lentz, R., Burger, T., Roy-Layinde, B., Lim, J., Zhu, R.M., Fan, D., Lenert, A., and Forrest, S.R. (2022). Air-Bridge Si Thermophotovoltaic Cell with High Photon Utilization. ACS Energy Lett. *7*, 2388–2392.
7. Wang, Z., Kortge, D., He, Z., Song, J., Zhu, J., Lee, C., Wang, H., and Bermel, P. (2022). Selective emitter materials and designs for high-temperature thermophotovoltaic applications. Sol. Energy Mater. Sol. Cell. *238*, 111554.

8. McSherry, S., Webb, M., Kaufman, J., Deng, Z., Davoodabadi, A., Ma, T., Kioupakis, E., Esfarjani, K., Heron, J.T., and Lenert, A. (2022). Nanophotonic control of thermal emission under extreme temperatures in air. Nat. Nanotechnol. *17*, 1104–1110.
9. Wang, J., Tang, X., Zhao, S., Deng, H., Ji, C., Wang, H., Liu, Y., Li, X., Lu, H., and Xu, Z. (2023). An Efficient Photon Utilization Radioisotope Thermophotovoltaic Based on Curled Reflectors. Energy Tech. *11*, 2201477.
10. Roy-Layinde, B., Lim, J., Arneson, C., Forrest, S.R., and Lenert, A. (2024). High-efficiency air-bridge thermophotovoltaic cells. Joule *8*, 2135–2145.
11. Chan, W.R., Bermel, P., Pilawa-Podgurski, R.C.N., Marton, C.H., Jensen, K.F., Senkevich, J.J., Joannopoulos, J.D., Soljačić, M., and Celanovic, I. (2013). Toward high-energy-density, high-efficiency, and moderate-temperature chip-scale thermophotovoltaics. Proc. Natl. Acad. Sci. USA *110*, 5309–5314.
12. Inoue, T., Koyama, T., Kang, D.D., Ikeda, K., Asano, T., and Noda, S. (2019). One-Chip Near-Field Thermophotovoltaic Device Integrating a Thin-Film Thermal Emitter and Photovoltaic Cell. Nano Lett. *19*, 3948–3952.
13. Lochbaum, A., Fedoryshyn, Y., Dorodnyy, A., Koch, U., Hafner, C., and Leuthold, J. (2017). On-Chip Narrowband Thermal Emitter for Mid-IR Optical Gas Sensing. ACS Photonics *4*, 1371–1380.
14. Davids, P.S., Kirsch, J., Starbuck, A., Jarecki, R., Shank, J., and Peters, D. (2020). Electrical power generation from moderate-temperature radiative thermal sources. Science *367*, 1341–1345.
15. Bermel, P. (2020). Capturing Waste Heat with CMOS Microelectronics. Joule *4*, 982–983.
16. Zuo, W., Li, D., E, J., Xia, Y., Li, Q., Quan, Y., and Zhang, G. (2023). Parametric study of cavity on the performance of a hydrogen-fueled micro planar combustor for thermophotovoltaic applications. Energy *263*, 126028.
17. Chan, W.R. (2015). High Efficiency Thermophotovoltaic Microgenerators (Massachusetts Institute of Technology).
18. Datas, A., Ramos, A., Martí, A., del Cañizo, C., and Luque, A. (2016). Ultra high temperature latent heat energy storage and thermophotovoltaic energy conversion. Energy *107*, 542–549.
19. LaPotin, A., Schulte, K.L., Steiner, M.A., Buznitsky, K., Kelsall, C.C., Friedman, D.J., Tervo, E.J., France, R.M., Young, M.R., Rohskopf, A., et al. (2022). Thermophotovoltaic efficiency of 40%. Nature *604*, 287–291.
20. Wang, H., Tang, X., Liu, Y., Xu, Z., Yuan, Z., Liu, K., Zhang, Z., and Jiang, T. (2020). Thermal Emission-Enhanced and Optically Modulated Radioisotope Thermophotovoltaic Generators. Energy Tech. *8*, 1901170.
21. Datas, A., and Martí, A. (2017). Thermophotovoltaic energy in space applications: Review and future potential. Sol. Energy Mater. Sol. Cell. *161*, 285–296.
22. Chubb, D. (2007). Fundamentals of Thermophotovoltaic Energy Conversion (Elsevier Science).
23. Planck, M. (1900). The theory of heat radiation. Entropie *144*, 164.
24. Tuley, R.S., and Nicholas, R.J. (2010). Band gap dependent thermophotovoltaic device performance using the InGaAs and InGaAsP material system. J. Appl. Phys. *108*, 084516.
25. Bauer, T. (2011). Thermophotovoltaics: Basic Principles and Critical Aspects of System Design (Springer Science & Business Media).
26. Roy-Layinde, B., Lim, J., Lenert, A., and Forrest, S.R. (2024). Integrated Air-Bridge Tandem Thermophotovoltaics with High Efficiency over a Broad Heat Source Temperature Range. ACS Energy Lett. *9*, 2832–2839.
27. Ferrari, C., Melino, F., Pinelli, M., Spina, P.R., and Venturini, M. (2014). Overview and Status of Thermophotovoltaic Systems. Energy Proc. *45*, 160–169.
28. Omair, Z., Scranton, G., Pazos-Outón, L.M., Xiao, T.P., Steiner, M.A., Ganapati, V., Peterson, P.F., Holzrichter, J., Atwater, H., and Yablonovitch, E. (2019). Ultraefficient thermophotovoltaic power conversion by band-edge spectral filtering. Proc. Natl. Acad. Sci. *116*, 15356–15361.
29. Fan, D., Burger, T., McSherry, S., Lee, B., Lenert, A., and Forrest, S.R. (2020). Near-perfect photon utilization in an air-bridge thermophotovoltaic cell. Nature *586*, 237–241.
30. Bierman, D.M., Lenert, A., Chan, W.R., Bhatia, B., Celanović, I., Soljačić, M., and Wang, E.N. (2016). Enhanced photovoltaic energy conversion using thermally based spectral shaping. Nat. Energy *1*, 16068.
31. Wang, Y., Liu, H., and Zhu, J. (2019). Solar thermophotovoltaics: Progress, challenges, and opportunities. APL Mater. *7*, 080906.
32. Pfiester, N.A., and Vandervelde, T.E. (2017). Selective emitters for thermophotovoltaic applications. Phys. Status Solidi *214*, 1600410.
33. Dyachenko, P.N., Molesky, S., Petrov, A.Y., Störmer, M., Krekeler, T., Lang, S., Ritter, M., Jacob, Z., and Eich, M. (2016). Controlling thermal emission with refractory epsilon-near-zero metamaterials via topological transitions. Nat. Commun. *7*, 11809.
34. Sakakibara, R., Stelmakh, V., Chan, W.R., Ghebrebrhan, M., Joannopoulos, J.D., Soljačić, M., and Čelanović, I. (2019). Practical emitters for thermophotovoltaics: a review. J. Photon. Energy *9*, 1.
35. Burger, T., Sempere, C., Roy-Layinde, B., and Lenert, A. (2020). Present Efficiencies and Future Opportunities in Thermophotovoltaics. Joule *4*, 1660–1680.
36. Jeon, N., Hernandez, J.J., Rosenmann, D., Gray, S.K., Martinson, A.B.F., and Foley IV, J.J. (2018). Pareto Optimal Spectrally Selective Emitters for Thermophotovoltaics via Weak Absorber Critical Coupling. Adv. Energy Mater. *8*, 1801035.
37. Lenert, A., Bierman, D.M., Nam, Y., Chan, W.R., Celanović, I., Soljačić, M., and Wang, E.N. (2014). A nanophotonic solar thermophotovoltaic device. Nat. Nanotechnol. *9*, 126–130.
38. Chirumamilla, M., Krishnamurthy, G.V., Knopp, K., Krekeler, T., Graf, M., Jalas, D., Ritter, M., Störmer, M., Petrov, A.Y., and Eich, M. (2019). Metamaterial emitter for thermophotovoltaics stable up to 1400 C. Sci. Rep. *9*, 7241.
39. Chirumamilla, M., Krishnamurthy, G.V., Rout, S.S., Ritter, M., Störmer, M., Petrov, A.Y., and Eich, M. (2020). Thermal stability of tungsten based metamaterial emitter under medium vacuum and inert gas conditions. Sci. Rep. *10*, 3605.
40. Chirumamilla, A., Yang, Y., Salazar, M.H., Ding, F., Wang, D., Kristensen, P.K., Fojan, P., Bozhevolnyi, S.I., Sutherland, D.S., Pedersen, K., and Chirumamilla, M. (2021). Spectrally selective emitters based on 3D Mo nanopillars for thermophotovoltaic energy harvesting. Mater. Today Phys. *21*, 100503.
41. Rinnerbauer, V., Ndao, S., Yeng, Y.X., Chan, W.R., Senkevich, J.J., Joannopoulos, J.D., Soljačić, M., and Celanovic, I. (2012). Recent developments in high-temperature photonic crystals for energy conversion. Energy Environ. Sci. *5*, 8815–8823.
42. Vaidhyanathan Krishnamurthy, G., Chirumamilla, M., Krekeler, T., Ritter, M., Raudsepp, R., Schieda, M., Klassen, T., Pedersen, K., Petrov, A.Y., Eich, M., and Störmer, M. (2023). Iridium-Based Selective Emitters for Thermophotovoltaic Applications. Adv. Mater. *35*, 2305922.
43. Krekeler, T., Rout, S.S., Krishnamurthy, G.V., Störmer, M., Arya, M., Ganguly, A., Sutherland, D.S., Bozhevolnyi, S.I., Ritter, M., Pedersen, K., et al. (2021). Unprecedented Thermal Stability of Plasmonic Titanium Nitride Films up to 1400 °C. Adv. Opt. Mater. *9*, 2100323.
44. Arpin, K.A., Losego, M.D., Cloud, A.N., Ning, H., Mallek, J., Sergeant, N.P., Zhu, L., Yu, Z., Kalanyan, B., Parsons, G.N., et al. (2013). Three-dimensional self-assembled photonic crystals with high temperature stability for thermal emission modification. Nat. Commun. *4*, 2630.
45. Chirumamilla, A., Ding, F., Yang, Y., Mani Rajan, M.S., Bozhevolnyi, S.I., Sutherland, D.S., Pedersen, K., and Chirumamilla, M. (2023). Tungsten nanodisc-based spectrally-selective polarization-independent thermal emitters. Sol. Energy Mater. Sol. Cell. *259*, 112449.
46. Chirumamilla, M., Roberts, A.S., Ding, F., Wang, D., Kristensen, P.K., Bozhevolnyi, S.I., and Pedersen, K. (2016). Multilayer tungsten-alumina-based

broadband light absorbers for high-temperature applications. Opt. Mater. Express *6*, 2704–2714.

47. Chang, C.-C., Kort-Kamp, W.J.M., Nogan, J., Luk, T.S., Azad, A.K., Taylor, A.J., Dalvit, D.A.R., Sykora, M., and Chen, H.-T. (2018). High-Temperature Refractory Metasurfaces for Solar Thermophotovoltaic Energy Harvesting. Nano Lett. *18*, 7665–7673.
48. Garín, M., Hernández, D., Trifonov, T., and Alcubilla, R. (2015). Three-dimensional metallo-dielectric selective thermal emitters with high-temperature stability for thermophotovoltaic applications. Sol. Energy Mater. Sol. Cell. *134*, 22–28.
49. Dyachenko, P.N., do Rosário, J.J., Leib, E.W., Petrov, A.Y., Störmer, M., Weller, H., Vossmeyer, T., Schneider, G.A., and Eich, M. (2015). Tungsten band edge absorber/emitter based on a monolayer of ceramic microspheres. Opt. Express *23*, A1236–A1244.
50. Leib, E.W., Pasquarelli, R.M., do Rosário, J.J., Dyachenko, P.N., Döring, S., Puchert, A., Petrov, A.Y., Eich, M., Schneider, G.A., Janssen, R., et al. (2016). Yttria-stabilized zirconia microspheres: novel building blocks for high-temperature photonics. J. Mater. Chem. C Mater. *4*, 62–74.
51. Arya, M., Ganguly, A., Krishnamurthy, G.V., Rout, S.S., Gurevich, L., Krekeler, T., Ritter, M., Pedersen, K., Störmer, M., Yu Petrov, A., et al. (2022). Which factor determines the optical losses in refractory tungsten thin films at high temperatures? Appl. Surf. Sci. *588*, 152927.
52. Vogel, N., Goerres, S., Landfester, K., and Weiss, C.K. (2011). A Convenient Method to Produce Close- and Non-close-Packed Monolayers using Direct Assembly at the Air–Water Interface and Subsequent Plasma-Induced Size Reduction. Macromol. Chem. Phys. *212*, 1719–1734.
53. Woolf, D.N., Kadlec, E.A., Bethke, D., Grine, A.D., Nogan, J.J., Cederberg, J.G., Bruce Burckel, D., Luk, T.S., Shaner, E.A., and Hensley, J.M. (2018). High-efficiency thermophotovoltaic energy conversion enabled by a metamaterial selective emitter. Optica *5*, 213–218.
54. Kim, J.H., Jung, S.M., and Shin, M.W. (2019). Thermal degradation of refractory layered metamaterial for thermophotovoltaic emitter under high vacuum condition. Opt. Express *27*, 3039–3054.
55. Shimizu, M., Kohiyama, A., and Yugami, H. (2018). Evaluation of thermal stability in spectrally selective few-layer metallo-dielectric structures for solar thermophotovoltaics. J. Quant. Spectrosc. Radiat. Transf. *212*, 45–49.
56. Cui, K., Lemaire, P., Zhao, H., Savas, T., Parsons, G., and Hart, A.J. (2018). Tungsten–Carbon Nanotube Composite Photonic Crystals as Thermally Stable Spectral-Selective Absorbers and Emitters for Thermophotovoltaics. Adv. Energy Mater. *8*, 1801471.
57. Rinnerbauer, V., Lenert, A., Bierman, D.M., Yeng, Y.X., Chan, W.R., Geil, R.D., Senkevich, J.J., Joannopoulos, J.D., Wang, E.N., Soljačić, M., and Celanovic, I. (2014). Metallic Photonic Crystal Absorber-Emitter for Efficient Spectral Control in High-Temperature Solar Thermophotovoltaics. Adv. Energy Mater. *4*, 1400334.
58. Jeon, N., Mandia, D.J., Gray, S.K., Foley, J.J., 4th, and Martinson, A.B.F. (2019). High-Temperature Selective Emitter Design and Materials: Titanium Aluminum Nitride Alloys for Thermophotovoltaics. ACS Appl. Mater. Interfaces *11*, 41347–41355.
59. Blandre, E., Vaillon, R., and Drévillon, J. (2019). New insights into the thermal behavior and management of thermophotovoltaic systems. Opt. Express *27*, 36340–36349.
60. Liu, X.J., Zhao, C.Y., Wang, B.X., and Xu, J.M. (2023). Tailorable bandgap-dependent selective emitters for thermophotovoltaic systems. Int. J. Heat Mass Tran. *200*, 123504.
61. Cao, S., Cai, Q., Zhang, Y., Zhang, Q., Ye, Q., Deng, W., and Wu, X. (2023). Emission mechanism and wide-angle adaptability of selective emitter based on combination of one and two-dimensional photonic crystals. Front. Energy Res. *10*, 995782.
62. Kohiyama, A., Shimizu, M., and Yugami, H. (2016). Unidirectional radiative heat transfer with a spectrally selective planar absorber/emitter for high-efficiency solar thermophotovoltaic systems. Appl. Phys. Express *9*, 112302.
63. Ferguson, L.G., and Dogan, F. (2001). A highly efficient NiO-Doped MgO matched emitter for thermophotovoltaic energy conversion. Mater. Sci. Eng., B *83*, 35–41.
64. Brace, D.B. (1901). The Laws of Radiation and Absorption: Memoirs by Prévost, Stewart, Kirchhoff, and Kirchhoff and Bunsen (American Book Company).
65. Siegel, R., and Howell, J. (1981). Thermal Radiation Heat Transfer (Hemisphere Publishing Corporation).
66. Peykov, D., Yeng, Y.X., Celanovic, I., Joannopoulos, J.D., and Schuh, C.A. (2015). Effects of surface diffusion on high temperature selective emitters. Opt. Express *23*, 9979–9993.
67. Shackelford, J.F., and Alexander, W. (2000). CRC Materials Science and Engineering Handbook (CRC press).
68. Salamon, K., Milat, O., Radić, N., Dubček, P., Jerčinović, M., and Bernstorff, S. (2013). Structure and morphology of magnetron sputtered W films studied by x-ray methods. J. Phys. D Appl. Phys. *46*, 095304.
69. Ilavsky, J., and Stalick, J.K. (2000). Phase composition and its changes during annealing of plasma-sprayed YSZ. Surf. Coating. Technol. *127*, 120–129.
70. Laukaitis, G., Dudonis, J., and Milcius, D. (2006). YSZ thin films deposited by e-beam technique. Thin Solid Films *515*, 678–682.
71. Pitcher, M.W., Ushakov, S.V., Navrotsky, A., Woodfield, B.F., Li, G., Boerio-Goates, J., and Tissue, B.M. (2005). Energy Crossovers in Nanocrystalline Zirconia. J. Am. Ceram. Soc. *88*, 160–167.
72. Diroll, B.T., Saha, S., Shalaev, V.M., Boltasseva, A., and Schaller, R.D. (2020). Broadband Ultrafast Dynamics of Refractory Metals: TiN and ZrN. Adv. Opt. Mater. *8*, 2000652.
73. Krishnamurthy, G.V., Chirumamilla, M., Rout, S.S., Furlan, K.P., Krekeler, T., Ritter, M., Becker, H.-W., Petrov, A.Y., Eich, M., and Störmer, M. (2021). Structural degradation of tungsten sandwiched in hafnia layers determined by in-situ XRD up to 1520° C. Sci. Rep. *11*, 3330.
74. Roberts, A.S., Chirumamilla, M., Wang, D., An, L., Pedersen, K., Mortensen, N.A., and Bozhevolnyi, S.I. (2018). Ultra-thin titanium nitride films for refractory spectral selectivity [Invited]. Opt. Mater. Express *8*, 3717–3728.
75. Rinnerbauer, V., Yeng, Y.X., Chan, W.R., Senkevich, J.J., Joannopoulos, J.D., Soljačić, M., and Celanovic, I. (2013). High-temperature stability and selective thermal emission of polycrystalline tantalum photonic crystals. Opt. Express *21*, 11482–11491.
76. Rinnerbauer, V., Ndao, S., Xiang Yeng, Y., Senkevich, J.J., Jensen, K.F., Joannopoulos, J.D., Soljačić, M., Celanovic, I., and Geil, R.D. (2013). Large-area fabrication of high aspect ratio tantalum photonic crystals for high-temperature selective emitters. J. Vac. Sci. Technol. B *31*, 011802.